Biorealistic Neuronal Temperature-Sensitive Dynamics within Threshold Switching Memristors: Toward Neuromorphic Thermosensation

Akhil Bonagiri, Sujan Kumar Das, Camilo Verbel Marquez, Armando Rúa, Etienne Puyoo, Shimul Kanti Nath, David Albertini, Nicolas Baboux, Mutsunori Uenuma, Robert Glen Elliman, et al.

Biorealistic Neuronal Temperature-sensitive Dynamics within Threshold Switching Memristors: Towards Neuromorphic Thermosensation

Akhil Bonagiri[1§], Sujan Kumar Das[2§], Camilo Verbel Marquez[3], Armando Rúa[3], Etienne Puyoo[4], Shimul Kanti Nath[2,5], David Albertini[4], Nicolas Baboux[4], Mutsunori Uenuma[6], Robert Glen Elliman[2], Sanjoy Kumar Nandi[2*]

[1]*Department of Electronics and Communication, Manipal Institute of Technology, Manipal Academy of Higher Education, Manipal-576104, Karnataka, India*

[2]*Department of Electronic Materials Engineering, Research School of Physics, Australian National University, Canberra, Australian Capital Territory, 2601, Australia*

[3]*Department of Physics, University of Puerto Rico, Mayaguez, PR, 00681 USA*

[4]*INSA Lyon, CNRS, Ecole Centrale de Lyon, Université Claude Bernard Lyon 1, CPE Lyon, INL, UMR5270, Villeurbanne, 69621 France*

[5]*School of Photovoltaic and Renewable Energy Engineering, University of New South Wales (UNSW Sydney), Kensington NSW 2052, Australia*

[6]*Information Device Science Laboratory, Nara Institute of Science and Technology (NAIST), Nara, 630-0192 Japan*

[§] Both authors contributed equally

E-mail: sanjoy.nandi@anu.edu.au

Abstract

Neuromorphic nanoelectronic devices that can emulate the temperature-sensitive dynamics of biological neurons are of great interest for bio-inspired robotics and advanced applications such as *in-silico* neuroscience. In this work, we demonstrate the biomimetic thermosensitive properties of two-terminal V_3O_5 memristive devices and showcase their similarity to the firing characteristics of thermosensitive biological neurons. The temperature-dependent electrical characteristics of V_3O_5-based memristors are used to understand the spiking response of a simple relaxation oscillator. The temperature-dependent dynamics of these oscillators are then compared with those of biological neurons through numerical simulations of a conductance-based neuron model, the Morris-Lecar neuron model. Finally, we demonstrate a robust neuromorphic thermosensation system inspired by biological thermoreceptors for bio-inspired thermal perception and representation. These results not only demonstrate the biorealistic emulative potential of threshold-switching memristors but also establish V_3O_5 as a functional material for realizing solid-state neurons for neuromorphic computing and sensing applications.

Keywords: Thermoreceptor, solid-state neuron, neuristors, negative differential resistance, vanadium oxides

1. Introduction

The neuromorphic computing paradigm aims to employ nonlinear bio-inspired processes, such as neuron-like spiking or synaptic learning, as computational and sensing primitives for achieving energy-efficient machine intelligence. One such process is the temperature-sensitive dynamics of biological neurons, which manifests as changes in spiking characteristics as a function of varying temperatures [1-2]. A process that plays a crucial role in many important neural functions such as thermal homeostasis [3], peripheral thermal sensation [4-5], and synchronization of the circadian rhythm [6], to name a few. Indeed, temperature perception is among the earliest sensory modalities observed in nature and can even be traced to relatively primitive microorganisms [7]. This is because it is essential for biological survival as it helps organisms react swiftly to noxiously hot or cold environments in order to protect themselves, and also helps to maintain the ideal body temperature to stabilize biological macromolecules and metabolic processes.

In mammals, thermosensation is facilitated through peripheral thermoreceptors that code absolute or relative changes in temperature by modulating the discharge rate of action potentials signaled to the Central Nervous System (CNS). In addition, thermal homeostasis is achieved by hypothalamic temperature-sensitive neurons that regulate the body temperature to maintain high metabolic efficiency by evoking various physiological and behavioral responses to correct any deviations from the ideal body temperature. Despite such ubiquity and significance in the neural system, research on understanding the temperature-dependent dynamics and characteristics of artificial neurons remains very limited. Most previous studies have focused on developing artificial neurons based on a range of materials, including insulator-metal transition (IMT) materials [8-10], spintronic magnetic tunnel junctions[11], and phase-change materials [12], and demonstrating their bio-plausibility by exhibiting the different spiking behaviors and inherent stochasticity [8, 13-15]. However, these typically only explore the single temperature (typically the

room-temperature) dynamics and do not delve into the temperature-dependent dynamics or limit the study to quasi-static current-voltage curves [16-17].

In this paper, we explore the effect of temperature on the spiking characteristics of V_3O_5-based threshold-switching neurons and reveal the close resemblance to their biological counterparts. Specifically, we show that the temperature-dependence of the spiking frequency and single spike characteristics match those of a biological neuron. We further demonstrate that tunable, temperature-dependent spiking windows can be achieved by applying different bias voltages to the device thereby providing the basis for neuromorphic temperature sensing with different receptive ranges for applications such as electronic skin and embedded sensing; More generally, such behavior paves the way for advanced systems-level applications like bioinspired temperature regulation and in-silico neuroscience.

2. Results and Discussion

2.1 V_3O_5 thin film characterization and switching mechanism

The two-terminal V_3O_5-based metal-oxide-metal (MOM) devices employed for this study have a planar structure, with the active device areas defined by a 10-150 μm gap between platinum electrodes of 20-50 μm width, as shown in Fig. 1(a). The device resistance has a strong temperature dependence, reflecting the temperature-dependent resistivity of the V_3O_5 film, which exhibits semiconductor-like behavior for temperatures in the range of 300-400K and undergoes an IMT in the range of 433±5K, during which the resistivity falls by an order of magnitude (Fig. 1(b)). The continuous nature of the IMT has previously been shown to result from inhomogeneities in the phase transition due to the polycrystalline nature of the V_3O_5 films [18]. It has been shown that the IMT in V_3O_5 is due to a change in the distribution of V^{3+} and V^{4+} ions from an ordered to a disordered state above the transition temperature[19-20]. This gives rise to a

reduction in the unit cell size by about 0.14%, which is much smaller than that observed in VO_2, where the IMT is associated with a Mott/Peierls mechanism[21].

The thermal coefficient of resistance (TCR), calculated using the formula $\mathrm{TCR} = d\mathrm{R}/\mathrm{R}dT$ where R is the resistance and T is the temperature, shows a distinct peak at 433 K due to the rapid change in resistance associated with the IMT; It is approximately constant at temperatures above and below the IMT, reflecting the near-exponential dependence of the resistance on temperature in the high and low resistance phases of V_3O_5 (Fig. 1(c). The magnitude of the TCR is ~3.4%.K^{-1} for the insulating phase of V_3O_5, which is similar to that of other materials (e.g., VO_2 has TCRs between -1.6 and -4.7 % K^{-1}) but it reaches a peak value of -12.8 % K^{-1} at 433 K [22-23]. This clearly identifies V_3O_5 as a potential functional material for bolometer-based applications [24-25].

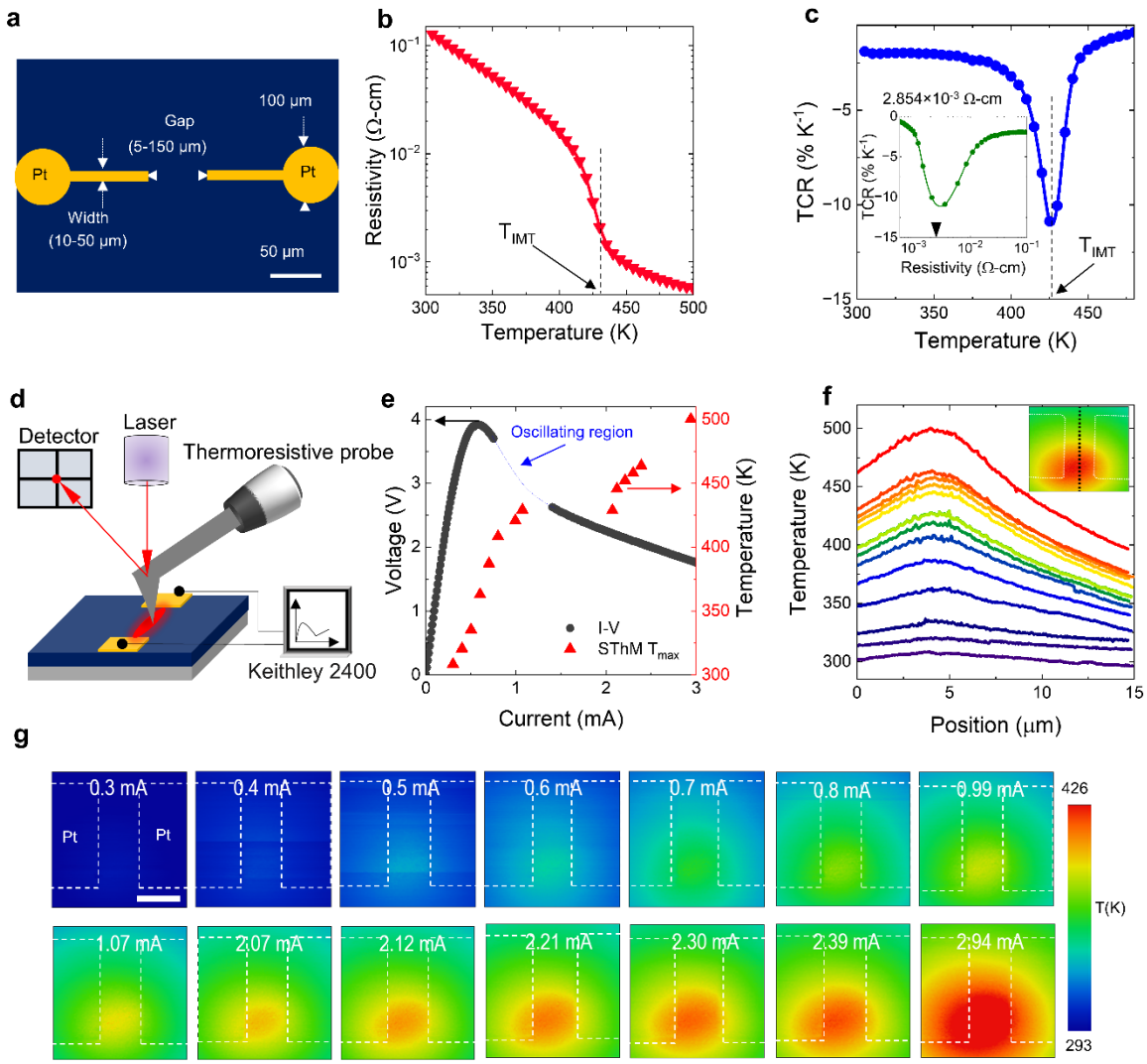

Figure 1. Temperature-dependent conductivity and switching mechanism: *(a) Schematic of the Pt/V_3O_5/Pt planar device structure. (b) Resistivity of the V_3O_5 film as a function of temperature for the heating cycle and, (c) variation of TCR with temperature (inset: variation of TCR with resistivity) for the corresponding V_3O_5 thin films. (d) In-situ SThM measurement setup with indicative circuit used for basic electrical measurements. (e) Ex-situ I-V characteristics and maximum temperature of the device area as a function of current during in-situ measurements. (f) Line trace plots showing the temperature profile across the middle of the device (half-way between the electrodes and perpendicular to the current flow)*

as a function of device current and (g) the corresponding 2D plot of temperature distribution of the device area obtained from in situ SThM measurements. The length of the scale bar is 5 μm.

We have previously shown that negative-differential resistance (NDR) in V_3O_5-based devices results from resistance changes induced by local Joule heating and that this can be amplified by non-linear current confinement effects [26]. To gain further insight into the impact of the device temperature on these processes, the current-voltage characteristics of Pt/V_3O_5/Pt devices (electrode gap 5 μm and electrode width 10 μm) were correlated with the temperature distribution within the device through in situ Scanning Thermal Microscopy (SThM) at room temperatures, as shown in Fig. 1(d). The I-V characteristics measured at room temperature exhibit two distinct regions: a smooth S-type NDR and a second oscillating region associated with the IMT for which no data points are included (Fig. 1(e)); The averaging of voltage oscillations has been shown to produce an apparent change in slope in the NDR region [26]. Corresponding temperature profiles taken across the middle of the device are shown as a function of device current in Fig. 1(f) and 2D temperature distributions of the device area are shown in Fig 1(g). Comparison of these data clearly shows that the onset of NDR (0.6 mA) occurs at a significantly lower temperature than the IMT. These results are consistent with our previous study and confirm that threshold switching and the onset of CC-NDR result from the temperature dependent conductivity of the insulating V_3O_5 phase, rather than an IMT [26].

To distill the impact of ambient temperature on the conduction mechanism, the current-voltage characteristics of Pt/V_3O_5/Pt devices were correlated with the temperature distribution within the device through in situ Middle Wavelength InfraRed (MWIR) spectroscopy at two different ambient temperatures, 303K and 333K (see Supplementary Information). In both cases, the temperature distribution is initially quite broad but narrows as the device is biased deeper into the NDR region (Point A) before becoming even more localized as the high-temperature region of the film undergoes an IMT (Point B). However, the

current is more localized at 303K than at higher temperature due to the lower resistivity of the surrounding V_3O_5 film at 333K (i.e., a larger fraction of the current is confined to the filamentary region at room temperature. See supplementary information for details).

2.2 V_3O_5 neuron and biological Morris-Lecar dynamics

To explore the room temperature oscillation dynamics of the V_3O_5 memristor, a series resistance R_L=2 kΩ and parallel capacitance C_p=1 μF were connected to the device in Pearson-Anson configuration and a DC bias of V_s=6 V was applied; The quasi-static I-V characteristics of the V_3O_5 memristor and a circuit diagram of the oscillator are shown in Figs. 2(a) and 2(b), respectively, and the corresponding current (through the device) and voltage (across the device) oscillations, are depicted in Fig. 2(c). For stable oscillation the load resistance must be greater than the maximum negative differential resistance (R_{NDR}) of the MOM device, i.e. (R_L>R_{NDR}), and the corresponding capacitance should be such that the electrical time constant (i.e. R_LC_p) is larger than the thermal time constant of the memristor (i.e. $R_{th}C_{th}$)[27]. For the given circuit parameters and operating conditions, the oscillation frequency was measured to be 0.40 kHz.

The temperature-dependent dynamics of biological neurons were calculated using the thermosenstive Morris-Lecar (M-L) neuron model; It is important to note that these waveforms are strikingly similar and analogous to the dynamics of membrane potential and recovery variables of the M-L model, respectively, as shown in a prior work [28]. The M-L model is a widely employed reduced two-variable version of the popular Hodgkin-Huxley description of a biological neuron, which was initially used to describe the membrane voltage dynamics of the barnacle giant muscle fiber [29]. It considers three ion channel currents: a) Fast-activating Calcium (Ca^{2+}) current, b) Delayed Potassium (K^+) current, and c) Leakage Current; with an underlying assumption that the dynamics of Ca^{2+} are on a much faster timescale than that of the K^+. The model is given by:

$$C\frac{dV}{dt} = -g_{Ca}M_{\infty}(V).(V - V_{Ca}) - g_K W(V - V_K) - g_L(V - V_L) + I_a \quad (1)$$

$$\frac{dW}{dt} = \eta.\tau_W(W_{\infty}(V) - W) \quad (2)$$

Where the variables V and W represent the membrane potential and the fraction of open K^+ channels respectively. V_{Ca}, V_K, V_L, g_{Ca}, g_K and g_L are the steady-state potentials and maximum conductance of calcium, potassium and leak ion channels, respectively. And η is the temperature factor, given by:

$$\eta = 3^{\frac{T-22}{10}} \quad (3)$$

where T is the temperature of the neuron in Kelvin. $M_{\infty}(V)$ and $W_{\infty}(V)$ are the voltage-sensitive opening probabilities for calcium and potassium channels, respectively, $\tau_W(V)$ denotes the voltage-dependent time constant of potassium activation gate. The equations for these voltage-sensitive quantities and the parameters used for simulation are given in the Supplementary Information.

The dynamics of the membrane potential (V) and fraction of open ion channels (W) predicted by the M-L model are shown in Fig. 2(d). Comparison with the dynamics of the V_3O_5 neuron in Fig. 2(c) shows that the dynamics of measured voltage (V_D) and current (I_D) are analogous to W and V in the M-L model, respectively [29]. As such, we considered the current through the device (I_D) as the *in-silico* equivalent of the biological action potential and used it to emulate neural temperature-dependent spiking. This contrasts with most previous studies [14, 30-32]. Further, to understand the temperature-dependent quasi-static and dynamic of V_3O_5 memristors, we used our previously developed lumped element circuit as shown in Fig. 2(e)[18]. It is apparent the simulation correctly describes the dynamic and NDR characteristics (see supporting information). Fig. 2(f) shows voltage- and current oscillation for an applied bias of V_S=6 V which is in quantitative agreement with experimental observations.

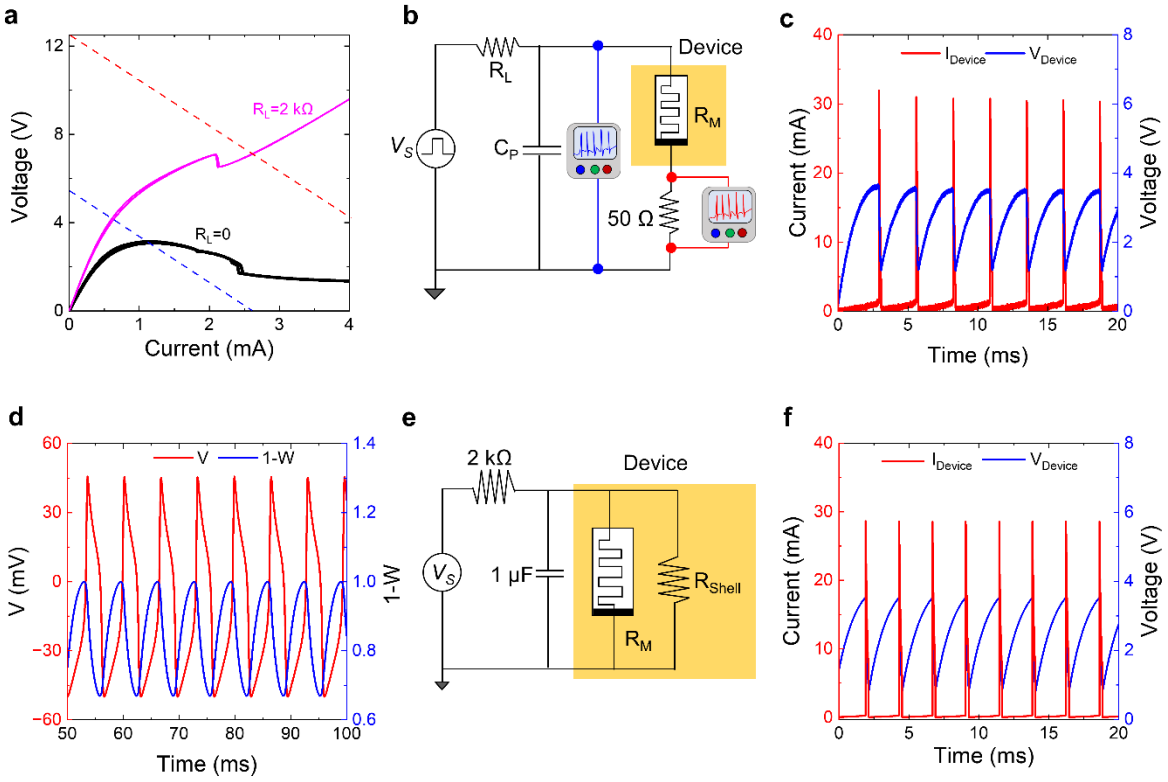

Figure 2. Experimental, calculated and simulated neurons: *(a) Experimental current-controlled I-V characteristics with and without load resistance. The load line passes through the NDR region of the I-V characteristics, leading to oscillations. (b) Schematic of the V_3O_5 oscillator circuit used for electrical measurements. (c) The experimental memristor current and voltage oscillation waveforms for V_S=6 V, R_L=2k Ω and C_p= 1 μF, at room temperature. (d) Calculated dynamics of the Morris-Lecar neuron* for a stimulus of 140 μA/cm^2. *(e) Lumped element model used to simulate dynamic characteristics and (f) simulated dynamic responses of V_{Device} and I_{Device} during a 20 ms 6 V pulse.*

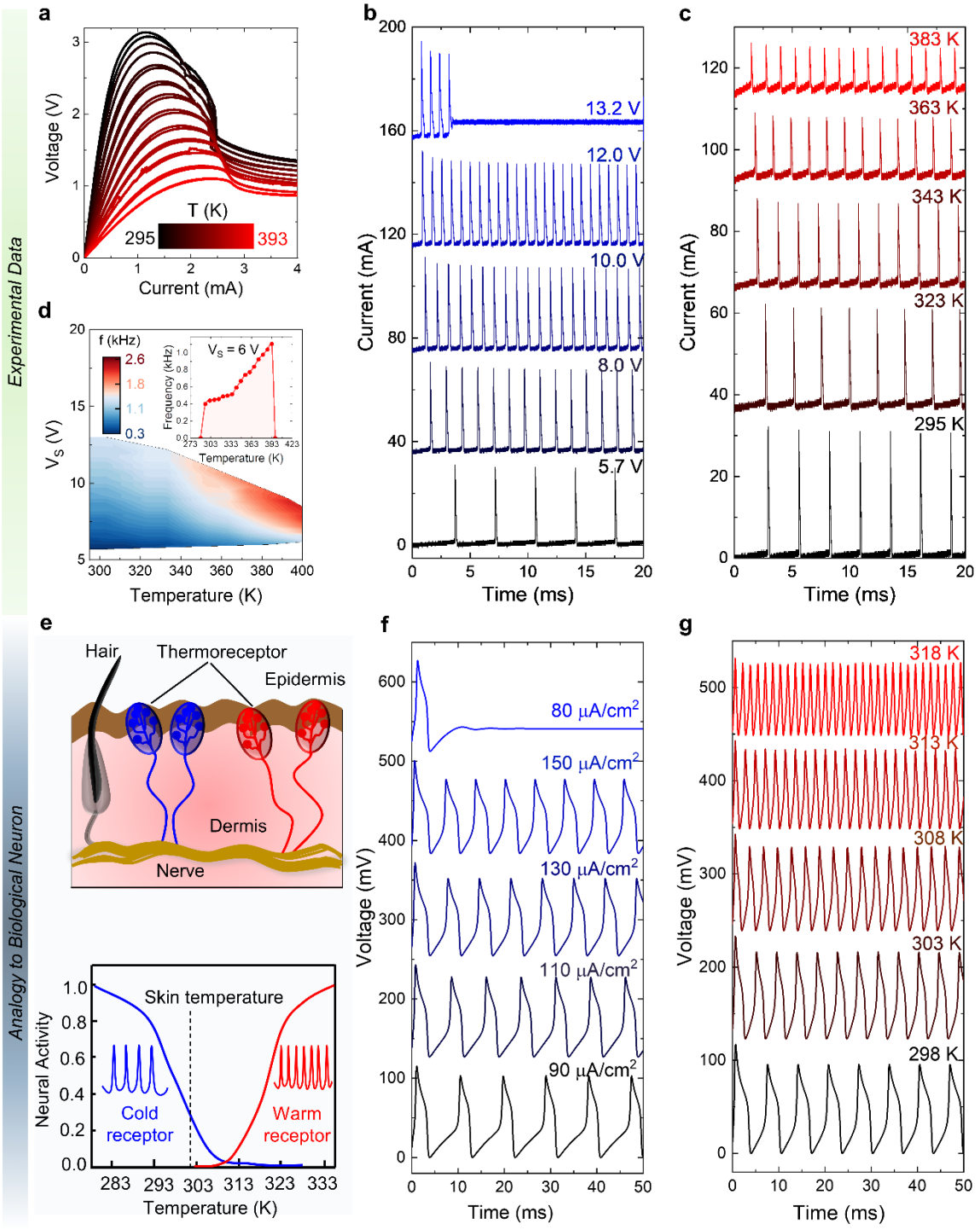

Figure 3. Analogy between experimental and biological neurons: *(a) Temperature-sensitive current-voltage characteristics of the V_3O_5 memristor (electrode gap 10 μm and electrode width 20 μm), in the range of temperatures 295-393K. (b) Measured temporal dynamics of the memristor current at different*

applied biases. (c) Measured temporal dynamics of the memristor current at different ambient temperatures. (d) Measured oscillation window frequency as a function of temperature and applied bias. Inset: The thermal frequency response curve at V_S=6 V (R_L=2 kΩ and C_p= 1 μF. (e) An illustration of the cross-section of the skin representing the biological thermoreceptors residing in the Dermis layer with spiking rate of biological thermal receptors in response to the stimulus temperatures. Redrawn and adapted with permission from reference[33]. (f,g) Simulated dynamics of Morris-Lecar neuron model at different applied biases (T=298 K) and different temperatures (I_a=140 μA/cm^2), respectively, corresponding to the V_3O_5 neuron dynamics in (b, c).

2.3 Artificial spiking thermoreceptor

To understand the temperature-dependent spiking of V_3O_5 neuristors, we first examine the effect of temperature on the CC-NDR of the V_3O_5 memristor. Fig. 3(a) shows the CC-NDR response of a Pt/V_3O_5/Pt device (electrode gap 10 μm and electrode width 20 μm) with increasing temperatures from 295K to 383K. The experimental threshold and hold voltages decrease monotonically over this temperature range from V_{th}=3.13 V to V_{th}=1.10 V and V_h=1.33V to V_h=0.86 V, respectively. Due to the greater temperature sensitivity of V_{th}, the hysteresis window between V_{th} and V_h also decreases with increasing temperature, typically reducing to zero near the IMT temperature (see supporting information). An effect that imposes a fundamental limit on using the memristor as an oscillator (or spiking thermoreceptor).

The dynamics and temperature-sensitivity of V_3O_5-based oscillators were measured using the circuit shown in Fig. 2(a), with R_L=2 kΩ, C_p=50 nF. For this circuit, stable self-oscillation occurs for voltages in the range between $V_{S,min}$ and $V_{S,max}$, where $V_{S,min} = V_{th} + (R_L + 50)I_{th}$ and $V_{S,max} = V_h + (R_L + 50)I_h$, respectively. Figs. 3(b) and 3(c) show typical results, corresponding to an applied bias range of

5.7-13.2 V (at T_{amb}=295 K) and device temperature range of 295-383 K (at V_S=6 V), respectively (see supporting information for further analysis).

In the latter case, the circuit begins to oscillate at a temperature of 295 K and continues to oscillate for temperatures up to 393 K, with the frequency increasing from 0.4 kHz to 1.1 kHz over this range, as summarized in the inset of Fig. 3(d). The circuit did not oscillate outside this temperature window for V_S=6 V, which can be attributed to the formation of a stable fixed point outside of the NDR region (to which the system settles, hence no oscillations) through a dynamical bifurcation [29]. This fixed point is located at the intersection of the device NDR and the circuit load line. The resistive phase of V_3O_5 corresponding to this fixed point depends on the temperature; in the above example, it corresponds to the insulating phases of V_3O_5 for temperatures T<295 K and to the metallic phase for T>393 K. The effects of both bias (V_S) and temperature T_{amb} on the oscillation frequency are summarized in Fig. 3(d). It is important to note here that the amplitude of spikes is determined by the resistance difference between the insulating and metallic states of the device. As the resistance of the insulating state is reduced at higher temperatures, the difference between that of the insulating and metallic states is also reduced, giving rise to a reduction in spike amplitude. The reduction in the resistance of the insulating state also reduces the RC relaxation time constant, which is manifest as a reduction in the width of the spikes. These characteristics are similar to those observed in NbO_x-based devices[10] and are accurately reproduced by simulated oscillation dynamics (see supporting information). The effect of scaling (i.e., smaller electrode gaps) on the NDR characteristics of devices is reported in a previous study[18], and its effect on oscillation dynamics is shown in the supporting information.

In mammals, environmental thermal signals are relayed from the periphery to the Central Nervous System by somatosensory thermoreceptor neurons as action potentials [5, 34]. These sensory neurons reside in the

dermis layer of the skin [top panel of Fig. 3(e)], collect information regarding the thermal environment and relay it to the dorsal horn in the spinal cord. There are four different types of thermal sensory neurons innervating the skin based on the type of ion channels embedded in their cell membranes, each of which differs in their thermal response curves due to the temperature-sensitive properties of the ion channels [bottom panel of Fig. 3(e)]. Different temperature ranges stimulate these four classes of cells and hence are used to discriminate between noxious hot, warm, cold, and noxious cold thermal stimuli. In humans, a skin temperature of 306 K is interpreted as neutral, and hence, these are stimulated depending on the temperature delta between the actual skin temperature and the neutral temperature. The thermal response curves of the typical sensory neurons are depicted in bottom panel of Fig. 3(e). The individual response curves of the biological neurons are qualitatively similar to that of the V_3O_5 neurons (Fig. 3(d), Inset) in that both of their spiking frequencies first gradually rise, peak and then fall. As demonstrated by Fig. 3(d), one can select the applied bias to adjust the temperature range the artificial neuron is receptive to. This is possible because the temperature window within which the V_3O_5 neurons spike can be tuned by adjusting the load line through the application of different biases, as the appearance of the unstable fixed point occurs in different temperature ranges for other load lines, leading to the bias-dependent characteristic frequency response curves. Hence, a single V_3O_5 neuron can mimic the activity of different types of biological thermo-sensory neurons just by adjusting the supply voltage V_S, which is significant for applications at large scale. In general, the thermal receptive ranges and shape of the V_3O_5 response curves can be easily modified by engineering the NDR characteristics and/or tuning the circuit parameters V_S, R_L and C_p. For instance, the max frequency can be modified by adjusting the parallel capacitance. The simulated dynamics of the M-L model as a function of applied current and temperature are shown in Fig. 3(f) and Fig. 3(g), respectively. The Morris-Lecar neuron (at T=298 K) oscillates for input current densities in the range of 90-150 $\mu A/cm^2$ (Fig. 3(f)) and the system transitions to a quiescent state, as shown

for a stimulus of 80 μA/cm^2, through a bifurcation mechanism analogous to that of the V_3O_5 neuron. The frequency of oscillation increases from ≈108 Hz at 90 μA/cm2 to ≈157 Hz at 150 μA/cm^2. The data in Fig. 3(g) (at an applied current density of 140 μA/cm^2) further demonstrates the strong temperature dependence of the spike frequency, with the oscillation frequency increasing from ≈151 Hz at 298 K to ≈588 Hz at 318 K. These dependencies on applied bias and temperature qualitatively match those of the V_3O_5 neuron shown in Fig. 3(b) and Fig. 3(c).

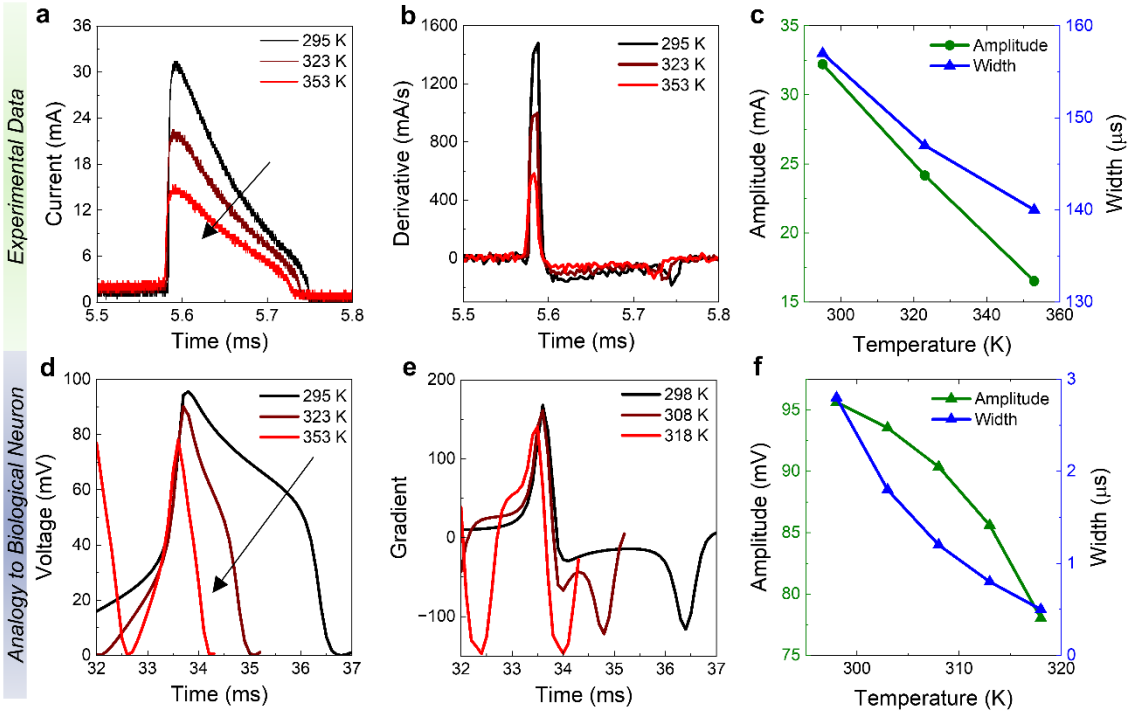

Figure 4. Effect of temperature on experimental and biological neurons: *(a) Effects of heating on the thermosensitive spikes generated by the V_3O_5 neuron, both the pulse amplitude and width decrease with increasing temperature. (b) The corresponding time derivatives of the current spikes in (a). c) The effects of heating on the spike amplitude and width are plotted against temperature, the temperature-dependence is qualitatively similar to that of (a). (d,e,f) Simulation results of the temperature-dependent Morris-Lecar neuron corresponding to (a,b,c).*

2.4 Biomimetic temperature-dependent individual spike dynamics

The overall shape of the action potential can play a role in neuronal information processing [35], synaptic dynamics [36], and synaptic transmission [37] so it is important to understand how the spike amplitude and width are affected by temperature. This was achieved by comparing the effect of temperature on the spike characteristics of V_3O_5 neurons with those of the temperature-dependent M-L model and action potential dynamics in animals.

Fig. 4(a) compares single spikes generated by the V_3O_5 neuron at three different temperatures (295 K, 323 K and 353 K), highlighting the reduction in spike amplitude with increasing temperature. The spikes have a characteristic sawtooth shape, with a fast rise time and a slower decay time, which is reflected in the time derivatives Fig. 4(b). The measurement of spike width was performed by evaluating the time difference between the maximum and minimum values of the spike gradients plotted in Fig. 4(b). This shows a relatively weak dependence on temperature compared to the amplitude, decreasing from 157 μs at 295 K to 140 μs at 353 K. The plots of the corresponding temperature-dependent amplitude and width measurements are summarized in Fig. 4(c). A similar analysis was conducted on the temperature-dependent Morris-Lecar neuron for comparison, and the results are depicted in Fig. 4(d-f). Over the temperature range of 298 K to 318 K, the M-L model spike amplitude drops from 95.63 mV to 78.03 mV, and the spike width decreases from 2.8 ms to 0.5 ms. The shape of the action potential is qualitatively similar to that of the V_3O_5 neuron but the temperature dependencies of the spike amplitude and width show significant differences; Spikes generated by the V_3O_5 neuron have a stronger temperature-dependent amplitude and a weaker temperature dependent width than predicted by the M-L model (See Figs. 4(c) and 4(f)). However, the thermosensitive spike dynamics of the threshold-switching neurons can be tuned by engineering the device and circuit parameters. i.e. The current spike amplitude directly corresponds to the quantity $I_{th,met} - I_{th,ins}$, where $I_{th,<phase>} = \frac{V_{th}}{R_{<phase>}}$. And the spike width is directly proportional

to the quantities $V_{th} - V_h$, R_S and C_p. It is important to note here that the amplitude of spikes is determined by the resistance difference between the insulating and metallic states of the device. As the resistance of the insulating state is reduced at higher temperatures, the difference between that of the insulating and metallic states is also reduced, giving rise to a reduction in spike amplitude. The reduction in the resistance of the insulating state also reduces the RC relaxation time constant, which is manifest as a reduction in the width of the spikes. These characteristics are similar to those observed in NbO_x-based devices[10] and are accurately reproduced by simulated oscillation dynamics (see supporting information). The effect of scaling (i.e., smaller electrode gaps) on the NDR characteristics of devices is reported in a previous study[18], and its effect on oscillation dynamics is shown in the supporting information.

Significantly, the spiking dynamics in the threshold-switching neurons are consistent with the results of experimental neuroscience measurements involving cell recordings from rat hypothalamus [1, 38], mouse hippocampus [39], cat motoneurons [40] and mouse skin sensory neurons [41]. For instance, *in vitro* measurements of the rat's hypothalamic suprachiasmatic nucleus[38] indicated that the average spike amplitude decreased by ≈10 mV and spike duration decreased by ≈0.12 ms as the temperature was increased from 305 K to 313 K.

2.5 Bio-inspired thermoreceptive sensing system

Given the thermoreceptive properties of individual threshold-switching neurons, as summarized in Fig. 3(a), it remains to examine the potential of a network of such neuristors in processing an applied spatial thermal stimulus and representing it as a discretized temperature map for neuromorphic sensing applications. In biology, projections of such a peripheral temperature map derived from the thermoreceptors and propagated to the central brain are functionally relevant for evoking behavioral responses to environmental temperature cues[42]. In fact, it has been shown in drosophila that silencing

hot/cold thermoreceptors leading to a distorted peripheral temperature representation, prevents the fly from avoiding harmful heat/cold[42-43]. Hence, guided by such principles, the neuromorphic thermosensation system discussed here can find applications in bio-inspired robotics or control systems running at edge.

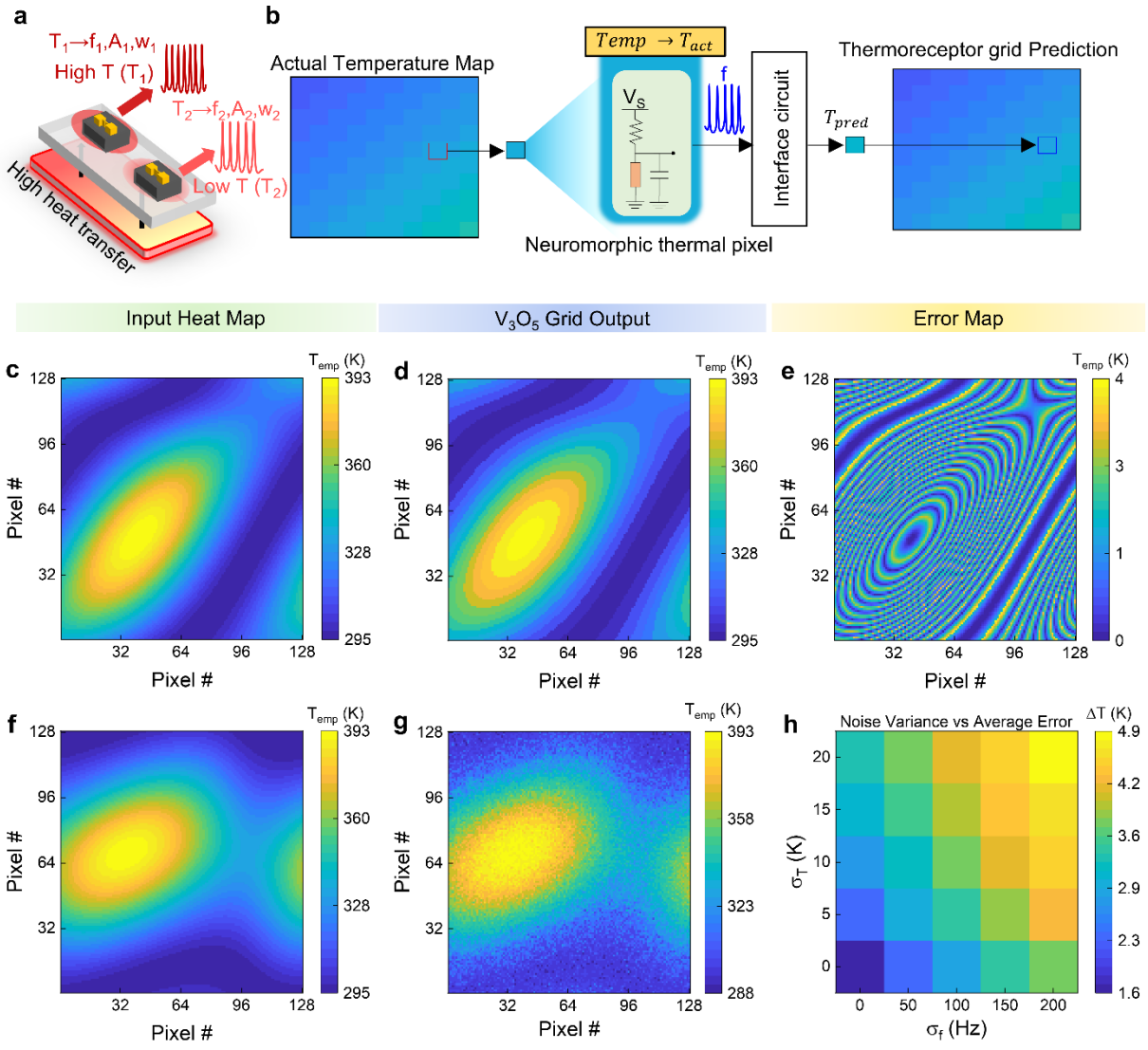

Figure 5. Simulated neuromorphic *thermoreception and temperature representation using two-terminal V_3O_5 memristors. (a) Schematic illustration of the thermoreceptive behavior exhibited by V_3O_5 neurons, temperature of the input stimuli modulates the neuron dynamics –-frequency f, amplitude A, and width w. b) Schematic illustration of the neuromorphic thermosensation and the thermal representation of a*

temperature gradient stimuli leveraging a 10×10 grid of thermal pixels consisting of memristive neurons. (c) A generated temperature gradient as the stimuli to the V_3O_5 grid. (d) The representation of the stimuli using a 128×128 grid of thermal pixels. (e) Pixel-wise absolute error between (c) and (d). (f,g) The response of the 128×128 thermal pixels grid (g) to another stimuli map (f), in presence of an additive temperature and frequency noise of variance σ_T =10 K and σ_f =200 Hz. (h) The effect of noise variance σ_T and σ_f on the average error of the grid representation across all pixels.

We propose and simulate a neuromorphic thermosensation system leveraging threshold-switching memristors consisting of a grid of thermal pixels where each cell consists of one V_3O_5 neuron (Fig. 5(a-b)). As conceptually illustrated in the figure, this grid essentially discretizes an applied spatial thermal stimulus where the resolution of the temperature map representation is limited by the size of an individual cell. Finally, the interface circuit samples the frequencies of neurons within a cell to yield the temperature of the corresponding cell. To demonstrate the ability of the system at a practical scale as a proof of concept, we adopted a coupled approach involving simulations guided by experimental measurements. Herein, we generated a randomized low-pass filtered heat stimuli map and applied it as an input to a grid of 128×128 cells, one neuron per cell with an applied bias of 6V. The experimental thermal response curve f (T), i.e., frequency as a function of temperature, of this neuron is depicted in the inset of Fig. 3(d), where the solid points represent the experimental measurements with linear interpolations in between them. In the simulation, we used these interpolated values (with an additive white Gaussian noise of mean $\mu_f = 0$ and variance σ_f) to estimate the output frequencies of the neuron for any stimuli temperature. This is not an unrealistic assumption because for repeated experimental measurements of a V_3O_5 neuron at the same temperature, the measured values will be distributed around a mean value and the Gaussian noise accounts for any frequency variations across multiple measurements. This assumption enabled us to keep the

simulation realistic while also drastically reducing the number of repeated measurements performed considering the analog thermal stimuli used and the scale of the network. Finally, in our example, the interface circuit comprised of minimization of root mean square error, i.e., the frequency error was computed between the output frequencies in simulation and experimental frequencies at each temperature and the interface output was the temperature with the least error. While we use simple error minimization, one can in principle use any other technique ranging from correlative measures to spiking neural network approaches.

Fig. 5(c) illustrates an applied thermal stimulus (295-393 K) to the network, Fig. 5(d) depicts the representation of the stimulus by the network, and Fig. 5(e) is the cell-wise absolute difference error. The network captures the details and essentially constructs a discrete approximation of the stimulus with an average absolute error of ≈1.61K across the grid and a maximum cell-wise error of ≈4.34 K. The number of levels in this discrete representation corresponds to the number of temperatures for which the experimental data was collected, 16 in our case. Hence, by increasing this number one can reduce the mean/maximum errors and improve the network approximation and quality of the representation.

Finally, to assert the robustness of this system against environmental variability and noise, we consider two noise sources, thermal noise ($\mu_T = 0, \sigma_T$) and frequency noise ($\mu_f = 0, \sigma_f$) and evaluate the performance of the system. Thermal noise was used to model any deviation between the stimulus and the ambient temperature as seen by the neuron which can stem from a range of practical causes ranging from undesired insulation to device wear off, and frequency noise was used to model the frequency deviations due to causes such as general environmental noise or NDR degradation. Figs. 5(f-g) depict the stimulus applied (295-393 K) and the response of the system for a noise of $\sigma_T = 10K$ and $\sigma_f = 100Hz$. Despite such high noise, especially thermal whose variance is ≈10% of the total temperature range of the stimulus, the system's representation captures the qualitative details with a mean error of ≈3.76 K across the grid.

Fig. 5(h) depicts the average error for different values of σ_T and σ_f. The mean error rises from 1.606K at no noise ($\sigma_T = 0K$, $\sigma_f = 0Hz$) to 4.897K at a very high noise ($\sigma_T = 20K$, $\sigma_f = 200Hz$). And this error can be further driven down by increasing the number of data points in the thermal response curve (16 points were used in our case). It can be seen that the variation of σ_f and σ_T does not have any disproportionate effect on the performance of the network, which implies that the system is robust against issues such as NDR degradation and device wear-off which is imminent over long-term usage. Furthermore, even a large thermal noise of $\sigma_T = 20\ K$ does not cause a great effect on the results of the network and causes a mean error of about ≈3.2-4.9 K depending on the σ_f.

To further increase the robustness of the system against noise, the number of neurons per cell can be increased where the thermal response curves of these neurons are distinct but overlapping. The response curves can be tuned by just altering the supply voltage of the neuron; hence at system-level, this scheme can be implemented by replicating the same neuron circuit and applying different biases to each of them. The use of multiple neurons with overlapping receptive ranges is to add redundancy and make the cell robust against noise, and this technique can also be leveraged to extend the overall receptive range of the cell. It is important to note here that the number of neurons used per cell and the overlap of their receptive ranges is an important consideration for robustness against noise. In general, a greater number of neurons and a high overlap between them maximize the thermoreceptor cell's robustness. Hence, one can trade-off between parameters such as the resolution of the thermal response curves, number of artificial thermoreceptors per cell, degree of overlap between their receptive ranges, and the size of the total grid based on desired design considerations like resolution of the output temperature map, robustness against noise, receptive range of the system, etc.

3. Conclusion

In conclusion, we have demonstrated the biomimetic thermosensitive properties of the V_3O_5-based neurons and revealed their connection to that of their biological counterparts. Specifically, it was shown that the emergent temperature-dependent dynamics of V_3O_5-based threshold-switching neurons can emulate the neural thermosensitive spiking observed in biological neurons. This was achieved by exploiting the temperature dependent characteristics of V_3O_5 memristors in a simple oscillator circuit and comparing the spike-dynamics with the predictions of the Morris-Lecar biological neuron model. It was further shown that a network of V_3O_5-based neurons could be used to process a spatial thermal stimulus for neuromorphic sensing applications. The similarity between artificial neurons based on threshold-switching devices and biological neurons clearly highlights their potential as neuromorphic sensory devices or as elements in large-scale neural dynamics simulation hardware for *in-silico* neuroscience.

Experimental Methods

A high quality V_3O_5 microcrystalline film of about ~500 nm thick was deposited on glass (SiO_2) substrate by DC pulsed magnetron sputtering. Two terminal planar devices with lengths 20 μm were made by depositing 100 nm of e-beam evaporated Pt contact pads patterned using standard lift-off process by e-beam lithography at 0.2 nm/s deposition rate having chamber pressure 1.28 mPa (9.6×10^{-6} Torr). PMMA was used as the electro-resist to pattern the electrodes during e-beam lithography. Before Pt electrode deposition a thin 5nm Ti adhesion layer was deposited by e-beam evaporation without breaking vacuum. The structure, composition, and morphology of the films were subsequently analysed using grazing incidence X-ray diffraction (GI-XRD), X-ray photoelectron spectroscopy (XPS), scanning electron microscopy (SEM), and transmission electron microscopy (TEM) (see supporting information)[18,44].

Rietveld refinement was used to determine the positions, heights, and widths of XRD peaks using the Fullprof software package[45-46].

Electrical measurements were performed in air using an Agilent B1500A semiconductor parametric analyser attached to a Signatone probe station with a heating-controlled sample stage. We waited for at least 5 mins after reaching the corresponding expected temperature prior to each measurement to stabilize the device temperature. To measure the oscillation dynamics using Pearson-Anson oscillator circuit a Rigol MSO-8104 4-channel digital oscilloscope was used to monitor the voltage drop across the 50 Ω monitor resistor in series with the device. In situ thermal imaging of the devices during electrical testing was undertaken using situ Scanning Thermal Microscopy (SThM) mapping using an SThM probe (VITA-DM-GLA from Brucker probes) mounted in a Dimension 3100 AFM and an InfraScope Middle Wavelength Infrared (MWIR) temperature mapping microscope employing by an InSb detector (Quantum Focus Instruments Co.)[47-49].

Supporting Information

This material is available free of charge via the Internet at http://pubs.acs.org.

Supporting figures including TEM, SEM and XPS analysis, DC and dynamic endurance, scaling effect on oscillation, model description and parameters.

Author Contributions

Akhil Bonagiri and Sujan Kumar Das contributed equally to this study.

Acknowledgments

We acknowledge access to NCRIS funded facilities and expertise at the ANU ion-implantation Laboratory (iiLab), a node of the Heavy Ion Accelerator (HIA) Capability at the Australian National University and

ACT node of the Australian National Fabrication Facility (ANFF). DA, NB and EP gratefully acknowledge the support from the Centre National de la Recherche Scientifique (CNRS) through the INSIS International Research Project Neurosensor. CVM and AR gratefully acknowledge the support from the National Science Foundation, through Award No. 2033328, and the Gordon and Betty Moore Foundation, grant doi:10.37807/GBMF12250, and from the UPRM College of Arts and Science.

Table of Content

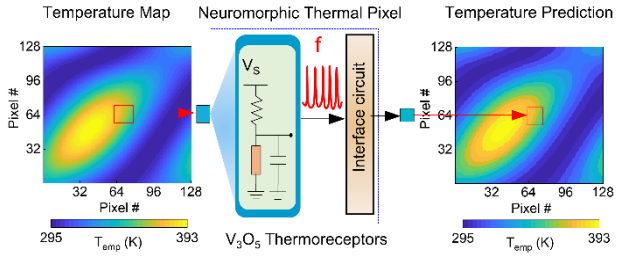

References

1. Boulant, J., Hypothalamic Neurons: Mechanisms of Sensitivity to Temperature A. *Annals of the New York Academy of Sciences* **1998,** *856* (1), 108-15.

2. Wang, H.; Wang, B.; Sharrock, M. F.; Llano, D., Brain Temperature and Its Fundamental Properties: A Review for Clinical Neuroscientists. *Frontiers in neuroscience* **2014,** *8*, 88894.

3. Robertson, R. M.; Money, T. G., Temperature and Neuronal Circuit Function: Compensation, Tuning and Tolerance. *Current opinion in neurobiology* **2012,** *22* (4), 724-34.

4. Vriens, J.; Nilius, B.; Voets, T., Peripheral Thermosensation in Mammals. *Nature Reviews Neuroscience* **2014,** *15* (9), 573-89.

5. Spray, D. C., Cutaneous Temperature Receptors. *Annual review of physiology* **1986,** *48* (1), 625-38.

6. Barrett, R. K.; Takahashi, J. S., Temperature Compensation and Temperature Entrainment of the Chick Pineal Cell Circadian Clock. *Journal of Neuroscience* **1995,** *15* (8), 5681-92.

7. Kobayashi, Y.; Harada, N.; Nishimura, Y.; Saito, T.; Nakamura, M.; Fujiwara, T.; Kuroiwa, T.; Misumi, O., Algae Sense Exact Temperatures: Small Heat Shock Proteins Are Expressed at the Survival Threshold Temperature in Cyanidioschyzon Merolae and Chlamydomonas Reinhardtii. *Genome biology and evolution* **2014,** *6* (10), 2731-40.

8. Yi, W.; Tsang, K. K.; Lam, S. K.; Bai, X.; Crowell, J. A.; Flores, E. A., Biological Plausibility and Stochasticity in Scalable Vo2 Active Memristor Neurons. *Nature Communications* **2018,** *9* (1), 4661.

9. Nandi, S. K.; Das, S. K.; Estherby, C.; Gentle, A.; Elliman, R. G., Understanding Modes of Negative Differential Resistance in Amorphous and Polycrystalline Vanadium Oxides. *Journal of Applied Physics* **2020,** *128* (24).

10. Nandi, S. K.; Li, S.; Liu, X.; Elliman, R. G., Temperature Dependent Frequency Tuning of Nbox Relaxation Oscillators. *Appl. Phys. Lett.* **2017,** *111* (20), 202901.

11. Grollier, J.; Querlioz, D.; Camsari, K.; Everschor-Sitte, K.; Fukami, S.; Stiles, M., Neuromorphic Spintronics. Nat. Electron. 3, 360–370. 2020.

12. Tuma, T.; Pantazi, A.; Le Gallo, M.; Sebastian, A.; Eleftheriou, E., Stochastic Phase-Change Neurons. *Nature nanotechnology* **2016,** *11* (8), 693-99.

13. Cheng, S.; Lee, M.-H.; Tran, R.; Shi, Y.; Li, X.; Navarro, H.; Adda, C.; Meng, Q.; Chen, L.-Q.; Dynes, R., Inherent Stochasticity During Insulator–Metal Transition in Vo2. *Proceedings of the National Academy of Sciences* **2021,** *118* (37), e2105895118.

14. Parihar, A.; Jerry, M.; Datta, S.; Raychowdhury, A., Stochastic Imt (Insulator-Metal-Transition) Neurons: An Interplay of Thermal and Threshold Noise at Bifurcation. *Frontiers in neuroscience* **2018,** *12*, 305614.

15. Bidoul, N.; Huet, B.; Ureña Begara, F.; Raskin, J.-P.; Flandre, D. In *Tuning the Stochasticity of Vo2 Neurons Firing-Threshold through Grain Size Engineering*, Proceedings of Neuromorphic Materials, Devices, Circuits and Systems (NeuMatDeCaS), 2023.

16. Bohaichuk, S. M.; Muñoz Rojo, M.; Pitner, G.; McClellan, C. J.; Lian, F.; Li, J.; Jeong, J.; Samant, M. G.; Parkin, S. S.; Wong, H.-S. P., Localized Triggering of the Insulator-Metal Transition in Vo2 Using a Single Carbon Nanotube. *ACS nano* **2019,** *13* (10), 11070-77.

17. Kim, B.-J.; Lee, Y. W.; Chae, B.-G.; Yun, S. J.; Oh, S.-Y.; Kim, H.-T.; Lim, Y.-S., Temperature Dependence of the First-Order Metal-Insulator Transition in Vo2 and Programmable Critical Temperature Sensor. *Applied physics letters* **2007,** *90* (2).

18. Das, S. K.; Nandi, S. K.; Marquez, C. V.; Rúa, A.; Uenuma, M.; Puyoo, E.; Nath, S. K.; Albertini, D.; Baboux, N.; Lu, T., Physical Origin of Negative Differential Resistance in V3o5 and Its Application as a Solid-State Oscillator. *Adv. Mater.* **2023,** *35* (8), 2208477.

19. Chudnovskii, F.; Terukov, E.; Khomskii, D., Insulator-Metal Transition in V3o5. *Solid State Commun.* **1978,** *25* (8), 573-77.

20. Aguilar-Maldonado, C.; Solana-Madruga, E.; Ritter, C.; Mentré, O.; Arévalo-López, Á. M., Abrupt Negative Thermal Expansion and Magnetic Structure of V3o5. *Chemistry of Materials* **2022,** *34* (11), 5294-300.

21. Kumar, S.; Strachan, J. P.; Pickett, M. D.; Bratkovsky, A.; Nishi, Y.; Williams, R. S., Sequential Electronic and Structural Transitions in Vo2 Observed Using X-Ray Absorption Spectromicroscopy. *arXiv preprint arXiv:1511.01918* **2015**.

22. Kittiwatanakul, S.; Sauber, N.; Cyberey, M.; Lichtenberger, A.; Weikle, R.; Lu, J. In *Tuning of Tcr in Poly-Crystalline Vo2 for Enhanced Ir Detection*, Image Sensing Technologies: Materials, Devices, Systems, and Applications V, SPIE: 2018; pp 38-43.

23. Wang, B.; Lai, J.; Li, H.; Hu, H.; Chen, S., Nanostructured Vanadium Oxide Thin Film with High Tcr at Room Temperature for Microbolometer. *Infrared Physics & Technology* **2013,** *57*, 8-13.

24. Zerov, V. Y.; Kulikov, Y. V.; Leonov, V.; Malyarov, V.; Khrebtov, I.; Shaganov, I., Features of the Operation of a Bolometer Based on a Vanadium Dioxide Film in a Temperature Interval That Includes a Phase Transition. *Journal of Optical Technology* **1999,** *66* (5), 387.

25. Gurvitch, M.; Luryi, S.; Polyakov, A.; Shabalov, A., Nonhysteretic Phenomena in the Metal–Semiconductor Phase-Transition Loop of $\Hbox {Vo} _ {2} $ Films for Bolometric Sensor Applications. *IEEE transactions on nanotechnology* **2010,** *9* (5), 647-52.

26. Rúa, A.; Díaz, R. D.; Kumar, N.; Lysenko, S.; Fernández, F. E., Metal-Insulator Transition and Nonlinear Optical Responseof Sputter-Deposited V3o5 Thin Films. *Journal of Applied Physics* **2017,** *121* (23).

27. Herzig, M.; Weiher, M.; Ascoli, A.; Tetzlaff, R.; Mikolajick, T.; Slesazeck, S., Multiple Slopes in the Negative Differential Resistance Region of Nbox-Based Threshold Switches. *Journal of Physics D: Applied Physics* **2019,** *52* (32), 325104.

28. Morris, C.; Lecar, H., Voltage Oscillations in the Barnacle Giant Muscle Fiber. *Biophysical journal* **1981,** *35* (1), 193-213.

29. Bonagiri, A.; Biswas, D.; Chakravarthy, S., Coupled Memristor Oscillators for Neuromorphic Locomotion Control: Modeling and Analysis. *IEEE Transactions on Neural Networks and Learning Systems* **2023**.

30. Yuan, R.; Duan, Q.; Tiw, P. J.; Li, G.; Xiao, Z.; Jing, Z.; Yang, K.; Liu, C.; Ge, C.; Huang, R., A Calibratable Sensory Neuron Based on Epitaxial Vo2 for Spike-Based Neuromorphic Multisensory System. *Nature communications* **2022,** *13* (1), 3973.

31. Zhang, X.; Zhuo, Y.; Luo, Q.; Wu, Z.; Midya, R.; Wang, Z.; Song, W.; Wang, R.; Upadhyay, N. K.; Fang, Y., An Artificial Spiking Afferent Nerve Based on Mott Memristors for Neurorobotics. *Nature communications* **2020,** *11* (1), 51.

32. Lappalainen, J.; Mizsei, J.; Huotari, M., Neuromorphic Thermal-Electric Circuits Based on Phase-Change Vo2 Thin-Film Memristor Elements. *Journal of Applied Physics* **2019,** *125* (4).

33. Gómez del Campo, A.; Viana, F., Detecting Warm Temperatures Is a Cool Kind of Thing. *Neuron* **2020,** *106* (5), 712-14.

34. Tansey, E. A.; Johnson, C. D., Recent Advances in Thermoregulation. *Advances in physiology education* **2015**.

35. Juusola, M.; Robinson, H. P.; de Polavieja, G. G., Coding with Spike Shapes and Graded Potentials in Cortical Networks. *Bioessays* **2007,** *29* (2), 178-87.

36. Niven, J.; Burrows, M., Spike Width Reduction Modifies the Dynamics of Short-Term Depression at a Central Synapse in the Locust. *Journal of Neuroscience* **2003,** *23* (20), 7461-69.

37. Ramezani, H.; Akan, O. B., Impacts of Spike Shape Variations on Synaptic Communication. *IEEE transactions on nanobioscience* **2018,** *17* (3), 260-71.

38. Burgoon, P. W.; Boulant, J. A., Temperature-Sensitive Properties of Rat Suprachiasmatic Nucleus Neurons. *American Journal of Physiology-Regulatory, Integrative and Comparative Physiology* **2001,** *281* (3), R706-R15.

39. Kim, J. A.; Connors, B. W., High Temperatures Alter Physiological Properties of Pyramidal Cells and Inhibitory Interneurons in Hippocampus. *Frontiers in cellular neuroscience* **2012,** *6*, 27.

40. Klee, M.; Pierau, F.-K.; Faber, D., Temperature Effects on Resting Potential and Spike Parameters of Cat Motoneurons. *Experimental Brain Research* **1974,** *19*, 478-92.

41. Boada, M. D.; Woodbury, C. J., Physiological Properties of Mouse Skin Sensory Neurons Recorded Intracellularly in Vivo: Temperature Effects on Somal Membrane Properties. *Journal of Neurophysiology* **2007,** *98* (2), 668-80.

42. Gallio, M.; Ofstad, T. A.; Macpherson, L. J.; Wang, J. W.; Zuker, C. S., The Coding of Temperature in the Drosophila Brain. *Cell* **2011,** *144* (4), 614-24.

43. Hamada, F. N.; Rosenzweig, M.; Kang, K.; Pulver, S. R.; Ghezzi, A.; Jegla, T. J.; Garrity, P. A., An Internal Thermal Sensor Controlling Temperature Preference in Drosophila. *Nature* **2008,** *454* (7201), 217-20.

44. Nath, S. K.; Das, S. K.; Nandi, S. K.; Xi, C.; Marquez, C. V.; Rúa, A.; Uenuma, M.; Wang, Z.; Zhang, S.; Zhu, R.-J.; Eshraghian, J.; Sun, X.; Lu, T.; Bian, Y.; Syed, N.; Pan, W.; Wang, H.; Lei, W.;

Fu, L.; Faraone, L.; Liu, Y.; Elliman, R. G., Optically Tunable Electrical Oscillations in Oxide-Based Memristors for Neuromorphic Computing. *Advanced Materials n/a* (n/a), 2400904.

45. Hewat, A.; David, W. I. F.; van Eijck, L., Hugo Rietveld (1932-2016). *Journal of Applied Crystallography* **2016,** *49* (4), 1394-95.

46. Roisnel, J., Fullprof. 98 and Winplotr: New Windows 95/Nt Applications for Diffraction Commission for Powder Diffraction. *International Union for Crystallography* **1998**.

47. Nandi, S. K.; Puyoo, E.; Nath, S. K.; Albertini, D.; Baboux, N.; Das, S. K.; Ratcliff, T.; Elliman, R. G., High Spatial Resolution Thermal Mapping of Volatile Switching in Nbo X-Based Memristor Using in Situ Scanning Thermal Microscopy. *ACS Appl. Mater. Interfaces.* **2022,** *14* (25), 29025-31.

48. Nandi, S. K.; Nath, S. K.; El-Helou, A. E.; Li, S.; Ratcliff, T.; Uenuma, M.; Raad, P. E.; Elliman, R. G., Electric Field-and Current-Induced Electroforming Modes in Nbo X. *ACS Appl. Mater. Interfaces.* **2020,** *12* (7), 8422-28.

49. Uenuma, M.; Ishikawa, Y.; Uraoka, Y., Joule Heating Effect in Nonpolar and Bipolar Resistive Random Access Memory. *Applied Physics Letters* **2015,** *107* (7).